Conceptual study of a morphing winglet based on unsymmetrical stiffness

Chen Wang, Hamed Haddad Khodaparast, Michael I Friswell

Abstract

Morphing technology has the potential to increase aircraft performance. Among the morphing technologies, the morphing winglet is a promising solution due to its small size and large effect on the aerodynamics. Morphing winglets have to carry the spanwise aerodynamic loads, with low weight and small size. This makes the design of a reliable morphing structure of great importance to realize a morphing winglet.

In this paper, a novel compliant structure is proposed based on the concept of unsymmetrical stiffness. The morphing winglet has to change its dihedral angle, and its stiffness has to be large enough to carry loads. While increasing the total stiffness, the allocation of the stiffness can be unsymmetrical, introducing deformation under a linear actuation force. If the total stiffness and its asymmetry are properly designed, the final deformation under both aerodynamic loads and actuation force can be optimized. The current study uses different composite layups of round corrugation structures to provide the stiffness asymmetry. A simplified model is developed to estimate the induced deformation and required actuation force. The deformation limit of the structure is also predicted using detailed finite element analysis.

To demonstrate the application of the morphing structure, the baseline design of a regional twin turboprop airliner is generated. A worm and rack actuation mechanism is also designed. For performance analysis, the weight due to the morphing winglet and its actuation system is estimated. The influence of retrofitting the baseline design is investigated to obtain a trade-off design for the morphing structure.

From the conceptual study, the simplified approach provides the basic properties of the morphing structure to retrofit the baseline aircraft, which highlights the feasibility of this novel concept although further study is still needed for its detailed design and analysis.

Key words: Conceptual study, Compliant Structure, Morphing winglet, Unsymmetrical stiffness

1. Introduction

The pursuit of better performance has continued since the dream of powered flight. The concept of a morphing aircraft or an adaptive wing [1] is one of the promising candidates which may change the way that the aircraft is designed and operated. The shape of conventional aircraft is only optimized for one flight condition while the morphing aircraft allows for active shape change under different flight conditions, which can provide additional aerodynamic benefits to the overall performance. Numerous morphing projects have been proposed, and the aircraft shape change may be used to categorize morphing concepts into wing span morphing [2, 3], camber morphing [4, 5], variable sweep morphing [6, 7], etc.

The development of wing tip devices can be traced to Lanchester's patent in 1897. But the early wing tip end plates were only useful at very high lift coefficients until Whitcomb proposed the winglet, which is a wing like surface at the wing tip [8]. The winglet is a small wing, which has an aerodynamic cross section and produces lift and drag. Installing the winglet can reduce the induced drag and weaken the wing tip vortices. A fixed winglet can only be optimized to meet the requirements of a specific flight condition. Also folding the wing tip can reduce the overall span to meet the airport restrictions.

The potential benefits of morphing technologies in the design of wing tip devices have aroused the attention of researchers. Bourdin et al. [9, 10] applied the morphing winglet for the control of morphing aircraft. Numerical studies and wind tunnel tests have validated the concept. Falcao et al. [11] proposed a morphing winglet mechanism for an unmanned aerial vehicle and an aero-structure optimization was performed to find the optimum wingtip configurations for different flight missions. A prototype of the morphing winglet was also constructed and tested experimentally to evaluate its actuation performance and dynamic response [12]. Smith et al. [13] performed a multi-objective optimization for multiple stages in a flight envelop, which has shown performance enhancement for a number of parameters. This work used the vortex lattice method for the aerodynamic analysis. To validate the low-fidelity method, computation work using a high-fidelity method has been undertaken together with the wind tunnel tests [14]. Another promising application of morphing wing tip devices is gust load alleviation. Guo et al. [15] proposed the passive twist wingtip, and the effect of folding wingtips in flight was investigated by Castrichini et al. [16] using a nonlinear hinge spring. There also remains some literature focused on the specific technology used in the morphing winglet. Li et al. [17] used a shape memory alloy spring as the actuator for a morphing winglet, which was able to change the cant angle. Daniele et al. [18] proposed an adaptive wing tip based on an inflatable system. Multi-stable structures were also investigated for their applications to morphing winglets by Mattioni et al. [19, 20]. There exist different ways to classify morphing wing tip devices, e.g. by the motivation, the application scenario, or the technology applied, which are briefly summarized in Figure 1. While there has been much progress to design the morphing winglet, some problems still remain. For example, the method to heat and cool down the shape memory alloys needs further investigation, especially when the required response speed is high. The application of the multi-stable structure could be limited since only discrete shape changes can be obtained. The conventional servo motor is a reliable actuation option but a morphing skin is still needed to provide a continuous aerodynamic surface for the morphing winglet.

The authors investigated the potential benefits of the morphing wing tip devices in an earlier study [21]. Different morphing variables were considered in two flight conditions, and the initial results showed a moderate performance increase, but also indicated that a reliable morphing structure is required. Therefore, this paper introduces a novel concept for a morphing winglet, and studies the design of the structure, which has the potential to overcome the difficulties in the design of the morphing winglet.

The proposed morphing winglet uses unsymmetrical stiffness of the compliant structure to achieve the change of dihedral angle. The change of lift to drag ratio and weight due to the retrofitted morphing winglet are compared to a baseline design. Since the spar is a primary structural member, the development of spanwise morphing technology is often very challenging when the lift is in the same direction of the required deformation.

This paper will first describe the concept of the unsymmetrical-stiffness induced deformation and derive the analytical solution for a simplified model in Section 2. Then, in Section 3 parametric studies will be conducted to show the influence of the unsymmetrical stiffness with both the actuation force

and the aerodynamic load taken into account. The model also considers the deformation limit of the proposed morphing structure.

In Section 4, a baseline design of a twin turboprop airliner is generated in order to demonstrate the application of the proposed morphing concept. Although adaptively changing the shape of the winglet could bring potential benefits to the aircraft, the weight increase due to the retrofitted winglet is one side effect that cannot be avoided. The weight significantly influences the overall performance. Although the drive in the aircraft industry is to reduce weight, the final decision should be made from the perspective of the performance to conduct flight missions, such as the amount of fuel consumed by a passenger airliner. One cannot exclude the existence of an aircraft that is heavier, but capable of satisfying different requirements, with potential improved performance, through the use of morphing technologies. It is necessary to consider both the positive effects of morphing technologies and the consequential weight change. Thus the estimate of aircraft weight is of great importance to the development of morphing aircraft although little attention has been paid to it. Skillen and Crossley [22] developed weight predictors for morphing aircraft. For the novel morphing winglet proposed here, the weight is estimated. The number of units of retrofitted morphing structures is taken into account to select an optimum trade-off.

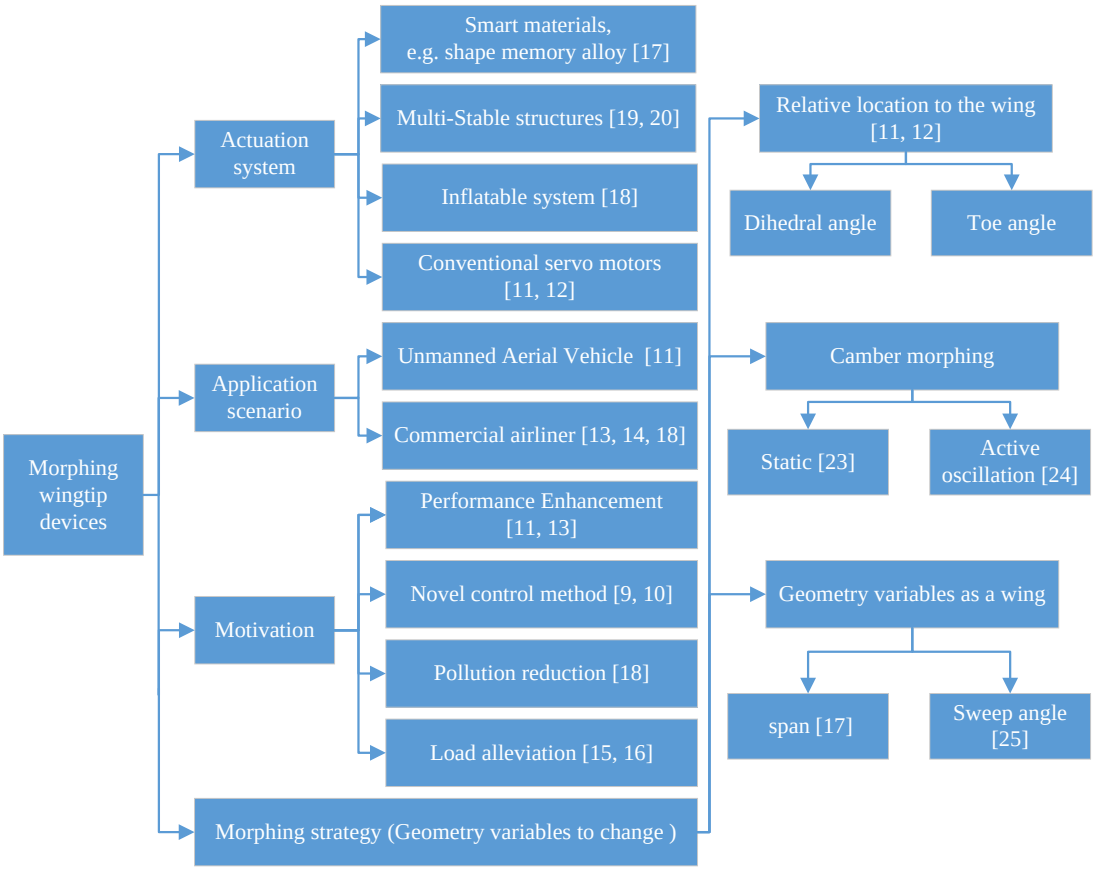

Figure 1. Classification of the morphing wing tip devices [23-25]

2. Concept of the compliant structure

2.1 A thermal analogy

In this paper, a novel compliant structure is proposed to transfer linear actuation to rotation of the

structure. Before the novel concept is introduced, the approach is motivated by analogy to the bimetallic strip. Figure 2(a) shows the deformation of the bimetallic strip, which has different thermal expansion coefficients for the two metal strips, namely strip 1 and strip 2. As shown, the different thermal expansions will cause different axial displacements between strip 1 and strip 2. Supposing strip 1 has a larger displacement, the connection between strip 1 and strip 2 will force the bimetallic strip to bend, balancing the differential displacement. By using the unsymmetrical thermal properties in the two strips, mechanical deformation can be obtained when the bimetallic strip is heated. Substituting the unsymmetrical thermal expansion coefficient with the unsymmetrical axial stiffness, deformation can also be obtained under actuation.

Compared to the bimetallic strip, the proposed compliant structure consists of the upper beam, the lower beam and the connection beam between them. The upper and lower beams can undergo extension deformation, but have different axial stiffnesses. When the actuation force is applied, the differential axial deformation between the upper and lower beam will cause the rotation of the structure. This concept is demonstrated in Figure 2(b). Although the upper and lower beams are both represented by beam-type structures in Figure 2(a), different forms can be used, such as the corrugation structure in Figure 2(b). Also the connection beam should be strong and stiff enough to transfer the loads. In the demonstration, the sample introduces stiffness asymmetry by making use of different corrugation shapes and sizes in the upper and lower corrugation structures. One end of the sample is fixed and the actuation force is applied on the other end, under which an induced rotation of the structure can be observed from the red dashed lines.

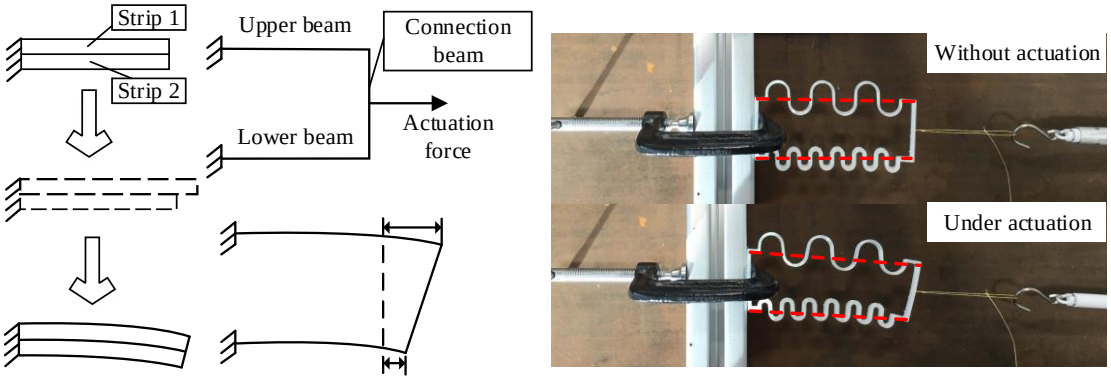

Figure 2. Concept of the compliant structure: (a) Analogy with the bimetallic strip, (b) Rotation of a demonstration sample

The above description indicates the potential feasibility of the proposed compliant structure. Since its deformation is induced by the actuation force, rather than temperature, it will be easier to control the final deformation and can be used under different environments. Also, the response speed of the structure under actuation will be faster and the structure can be less sensitive to the change of the environment temperature. This paper will demonstrate its application to morphing aircraft. It should be noted that the proposed compliant structure can also be applied in other industrial fields, such as robotics. The research on the novel concept can also help to develop the design theory of compliant structures.

2.2 Simplified 2-dimensional model

In the current study, the compliant structure is regarded as a frame, whose upper and lower members

can both extend and bend, but will still follow small deformation theory. Figure 3 shows the 2-dimensional (2D) model that represents the deflection under external forces. The 2D model consists of the upper, lower and connection beams labelled *AB*, *DC* and *BC* respectively. Beam *AB* and *DC* can undergo both axial deformation and bending. Beam *BC* is assumed to be rigid compared to beams *AB* and *DC*.

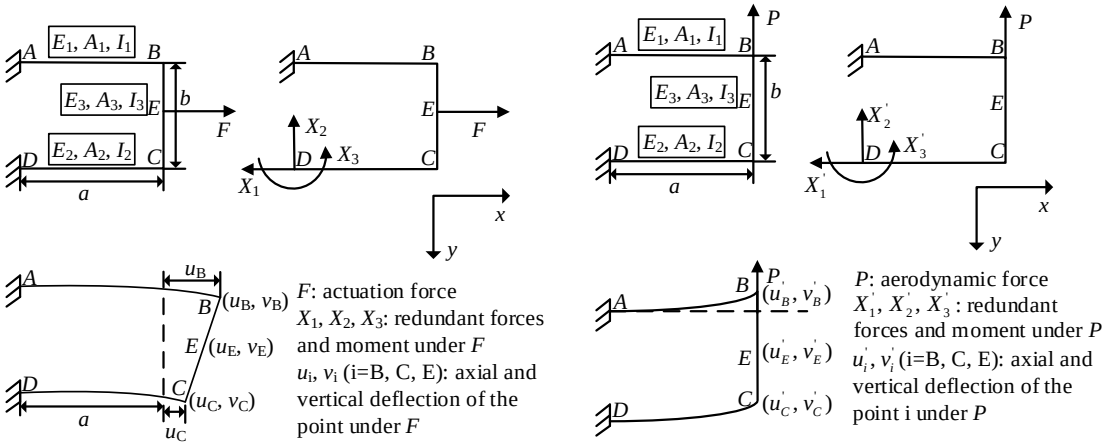

Figure 3. Deflection of structure: (a) under actuation force, (b) under aerodynamic force

The Young's modulus, area and second moment of area of beams *AB*, *DC* and *BC* are represented by E_1, A_1, I_1, E_2, A_2, I_2, E_3, A_3, I_3 respectively. The length and height of the 2D model are represented by *a* and *b* respectively. The structure is regarded as a frame under the actuation force *F*. To simplify the model, the actuation force is currently applied in the middle of beam *BC*, namely point *E*, while the deflection for other actuation locations can be found following the same method. Since the structure is statically indeterminate, the deflection can be calculated by the force method [26] and a detailed explanation can be found in the appendix. X_1, X_2 and X_3 are the redundant forces and moment applied at point *D* to make the structure statically-determinate and satisfy the deformation compatibility conditions at point *D*, i.e.

$$\begin{aligned} u &= -\frac{Fa}{E_1A_1} - \frac{Fab^2}{2E_1I_1} + \left(\frac{ab^2}{E_1I_1} + \frac{a}{E_1A_1} + \frac{a}{E_2A_2}\right)X_1 + \frac{a^2b}{2E_1I_1}X_2 - \frac{ab}{E_1I_1}X_3 = 0 \\ v &= -\frac{a^2b}{4E_1I_1}F + \frac{a^2b}{2E_1I_1}X_1 + \left(\frac{a^3}{3E_1I_1} + \frac{a^3}{3E_2I_2}\right)X_2 - \left(\frac{a^2}{2E_1I_1} + \frac{a^2}{2E_2I_2}\right)X_3 = 0 \\ \alpha &= \frac{Fab}{2E_1I_1} - \frac{ab}{E_1I_1}X_1 - \left(\frac{a^2}{2E_1I_1} + \frac{a^2}{2E_2I_2}\right)X_2 + \left(\frac{a}{E_1I_1} + \frac{a}{E_2I_2}\right)X_3 = 0 \end{aligned} \tag{1}$$

where *u*, *v*, α are the displacements in *x* and *y* direction, and the rotation at point *D* respectively. Matlab® [27] symbolic calculation is used to obtain the redundant forces and moment, which are then used to calculate the displacement of the other points. The displacement of point *E* can be expressed as

$$\begin{aligned} u_E &= \frac{F}{2}a\frac{2E_1I_1 + 2E_2I_2 + b^2(E_1A_1 + E_2A_2)/2}{K_t} \\ v_E &= \frac{Fba^2}{2}\frac{E_2A_2 - E_1A_1}{2K_t} = \frac{Fba^2}{4K_tE_1A_1}\left(r_s - 1\right) \end{aligned} \tag{2}$$

where the term K_t is the combination of the axial and bending stiffness of both upper and lower beams, which can be expressed as

$$K_t = E_1A_1E_1I_1 + E_2A_2E_2I_2 + E_1A_1E_2I_2 + E_1I_1E_2A_2 + E_1A_1E_2A_2b^2 \tag{3}$$

And the ratio r_s is the axial stiffness ratio between the lower and upper beam as

$$r_s = \frac{E_2 A_2}{E_1 A_1} \tag{4}$$

According to Equation (2), no vertical deflection can be obtained when the ratio r_s is equal to 1, which means the upper and lower beam have the same axial stiffness.

To verify the expression, the analytical results are compared with the finite element method in the commercial software Abaqus® [28] as shown in Figure 4. In this case, the length, width and height of the structure are all equal to 0.1 m and the actuation force is 1000 N. The mesh size is selected at 0.002 m and the model uses 7500 S4R general purpose shell elements. The general purpose shell element can simulate both thin and thick plates, and the use of the shell elements allows for the fast model building for future study of 3-dimensional cases by modifying the script files of the Abaqus® models.

At first, the induced displacement is calculated using aluminum beams but with different thickness. The upper beam has a rectangular profile, whose thickness is fixed at 1mm, while the thickness of the lower beam is increased. The analytical method is then compared to a finite element model of composite plates. The composite layup is symmetric and the composite ply angle is 0 or 90 degrees in turn with respect to the x axis. The modulii E_1 and E_2 are obtained from the effective modulus in the x direction of the composites. The composite in the upper part is made of 10 plies while the number of plies of the lower composite varies from 10 to 250. The composites properties are from reference [29] and the ply thickness is 0.125 mm. The micromechanical models in [29] are used to calculate the elastic modulii and ultimate strength of the lamina. Although experiments should be performed to test the composites, the current approach provides reasonable material data for the conceptual level study. Table 1 provides the material properties used and Table 2 summarizes the lamina properties when the matrix volume fraction is 0.7.

Matrix properties (Epoxy)		Fiber properties (Fiber glass)	
Axial modulus (GPa)	3.4	Axial modulus (GPa)	85
Poisson's ratio	0.3	Poisson's ratio	0.2
Shear modulus (GPa)	1.308	Shear modulus (GPa)	35.42
Tensile strength (MPa)	72	Tensile strength (MPa)	1550
Compressive strength (MPa)	102	Compressive strength (MPa)	1550
Shear strength (MPa)	34	Shear strength (MPa)	35

Table 1. Properties of the matrix and fiber

Elastic moduli (GPa)		Ultimate strength (MPa)	
Axial modulus E_1	27.9	Axial tensile strength X_t	501.84
Transverse modulus E_2	4.78	Axial compressive strength X_c	98.0
Poisson's ratio v_{12}	0.27	Transverse tensile strength Y_t	41.17
Shear modulus G_{12}	1.84	Transverse compressive strength Y_c	58.26
		In-plane shear strength S	19.36

Table 2. Properties of the composite lamina

Figure 4 shows that the linear actuation applied at beam *BC* is able to induce the rotation of the structure. When the upper and lower beams have the same axial stiffness no rotation is obtained and with the increase of the lower beam stiffness the vertical deflection will increase first and then reduce

under the same actuation force. The initial increase is due to the increasing stiffness asymmetry while the deflection would be reduced inevitably since an infinite stiffness of the lower beam would lead to zero deflection. For the isotropic aluminum plate, the error between the analytical solution and the finite element method is smaller than 3%, and for the composite plate, the error is smaller than 1%, which means the 2D simplified model provides reasonable accuracy.

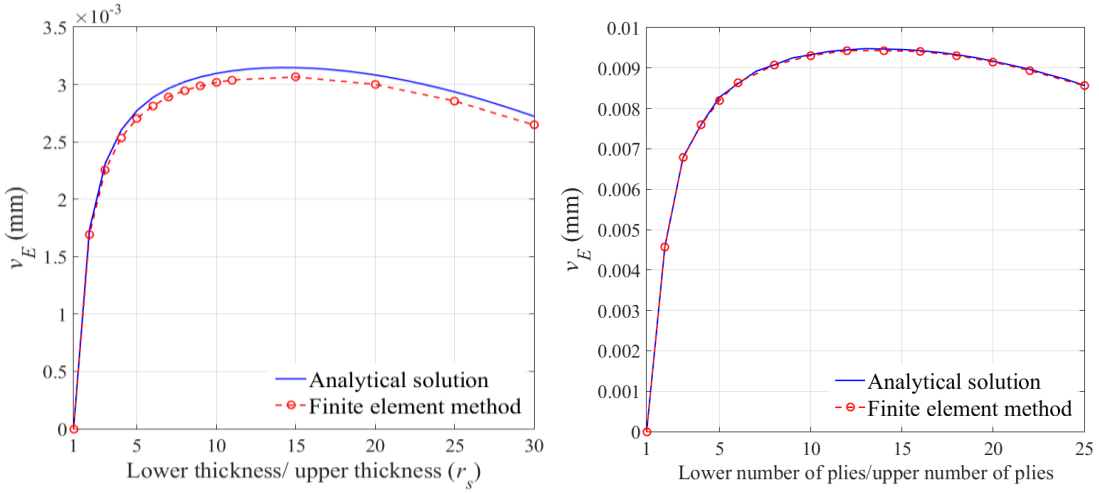

Figure 4. Actuated deflection of: (a) Aluminum structure, (b) Composite structure

3. Application to the morphing structure

3.1 Influence of unsymmetrical stiffness

As a morphing structure, the proposed compliant structure can be used to change the dihedral angle if it is installed spanwise. The morphing structure needs to change shape and maintain the geometry under aerodynamic loads simultaneously.

To find the influence of the unsymmetrical stiffness on the capability of carrying aerodynamic loads, the deformation under aerodynamic loads is calculated using the simplified model in section 2.2. As shown in Figure 3(b), the aerodynamic loads are concentrated at point *B* as a vertical force *P*. The displacement of point *E* under the aerodynamic force is calculated in the same way as the displacement of point *E* under the actuation force as

$$\begin{aligned} u_E^{'} &= \frac{E_1A_1 - E_2A_2}{4K_t} Pa^2b \\ v_E^{'} &= \frac{\left(3E_1A_1E_2A_2b^2 / K_t - 4\right)}{12(E_1I_1 + E_2I_2)} Pa^3 \end{aligned} \tag{5}$$

In contrast to the actuation force case, the vertical deflection is not related to the difference in the axial stiffnesses in the upper and lower beams. The change in the vertical deflection under aerodynamic force will be different to that under actuation force if the stiffness asymmetry is increased, which allows the decoupling of the vertical deflections under actuation and aerodynamic forces.

To make use of the stiffness asymmetry, a proper form of the upper and lower structure should be selected. According to Equation (2), there is no strict rule for the form of the upper and lower structure only that they can provide unsymmetrical stiffness. Isotropic or anisotropic plates can be used, as used in the verification examples in Figure 4. In the demonstration experiment, corrugated structures are used in the upper and lower beams. The corrugated structure has been investigated extensively for its

application in morphing aircraft in recent years, such as [30, 31]. The corrugated structure has a low axial elastic modulus and a large deformation limit due to its anisotropic properties. By substituting the Young's modulii, E_1 and E_2, with the equivalent modulus in the corresponding direction, the deflection of the morphing structure can be calculated by an analytical approximation. It should be noted that since the corrugated panel has a fixed boundary condition, the corrugated panel should be fixed carefully to eliminate the extension and bending coupling of corrugated panels. Since the focus of this paper is to introduce the conceptual study of the novel compliant structure, the detailed analysis and method will be reported in another paper. In the current study the equivalent properties of the corrugated structure are obtained using the homogeneous method proposed by Xia et al. [32]. The round corrugation is used and the geometry definition is shown in Figure 5(a). The corrugation structure is made of the composites described in Table 2. Detailed finite element models are created first to compare the equivalent modulus to the homogeneous method in Figure 5(b) and to obtain the deformation limit for the next section. The models are created in Abaqus® and each finite element model has 4 round corrugations. The model is pinned at one end and axial displacement is applied at the other end, from which the reaction forces are obtained to calculate the equivalent modulus. The S4R shell elements are used and the mesh size is 0.001 m to ensure the geometry of the round corrugation is produced accurately. The results from the equivalent method have small error (less than 1%) compared to the detailed finite element analysis.

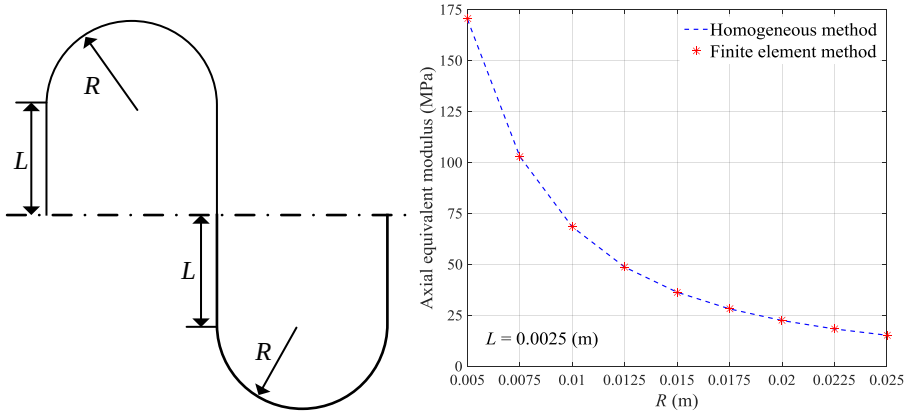

Figure 5. (a): Geometry of one round corrugation, (b): Equivalent modulus of the round corrugation

The stiffness asymmetry can be introduced by either changing the shape of the round corrugation, i.e. L and R, or changing the thickness, or number of plies and ply angle if composite material is used. To simplify the problem, the shape is fixed at R = 0.025 m and L = 0.01 m in the following study, and the stiffness in the lower corrugation structure is changed by changing the number of plies while fixing the upper properties. The length, width and height of the compliant structure are all equal to 0.1 m.

Parametric studies are conducted to show the influence of the unsymmetrical stiffness. Figure 6(a) shows the rotation angle under actuation and aerodynamic forces. The rotation angle is calculated according to the displacements of point E. The aerodynamic force is fixed at 100 N, and the rotation angles under different actuation forces are considered. The simulated actuation and aerodynamic forces are representative and used to demonstrate the asymmetric stiffness concept; in a morphing application the estimated aerodynamic forces would be used and the actuation force would be optimized. The x axis represents the number of plies in the lower composite layup. With the increase of this number both the total stiffness and stiffness asymmetry of the structure are increased. With the increase of the total stiffness the rotation under aerodynamic force declines sharply while the rotation angle under actuation

force will climb first. If enough stiffness is added to the lower corrugation, the rotation angle caused by the actuation force will be greater than that of the aerodynamic force.

From another perspective, the required angle, which is the rotation angle for a specific aerodynamic force, determines the required actuation force. Different to the conventional structure the actuation force actively takes part in determining the structure's geometry. As shown in Figure 6(b), different actuation forces are required for different required angles although the aerodynamic force is fixed at 100 N. When the number of plies in the lower composite is too small, the total stiffness of the structure will be too small and the required angle cannot be achieved. If the required angle is 0, which means the actuation force is only used to maintain the geometry under aerodynamic force, the required actuation force will be reduced continuously by increasing the stiffness in the lower part. However if the required angle is larger than 0, the actuation force will climb again after the initial decline. Since both the stiffness asymmetry and the total stiffness of structure affect the final deformation, the final deflection will reduce if the total stiffness reaches an adequate level although the stiffness asymmetry still exists.

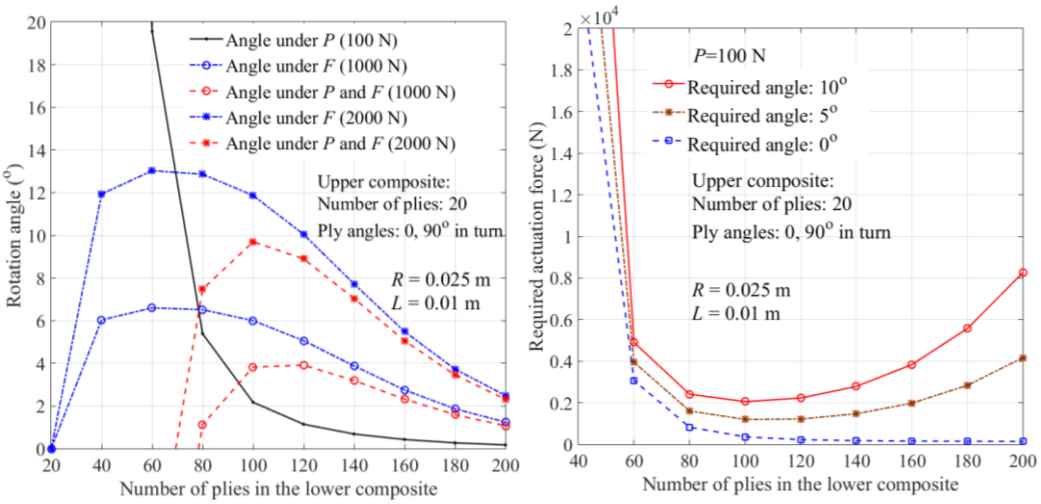

Figure 6. (a) Rotation angle under actuation force and aerodynamic force;
(b) Required actuation force for the required rotation angle

From the above analysis a high total stiffness of the morphing structure is useful to reduce the rotation under aerodynamic force while a properly selected stiffness asymmetry helps to induce the required rotation angle. The above analysis used the same composite ply angle for both the upper and lower corrugation structure. The unsymmetrical stiffness is only introduced by changing the number of plies in the lower part while a larger stiffness asymmetry can be achieved by using different ply angles. For instance the following analysis shows the rotation angle and required actuation with a more flexible upper composite layup, where the ply angles are all equal to 90 degrees. Of course this layup will not be practical in real applications but the extreme stiffness anisotropy is used here to demonstrate the effect of changing the layup.

Figure 7 shows that the rotation angle can be obtained even though the number of plies in the lower composite is still 20 due to the different composite ply angle. Although the more flexible upper part leads to the larger rotation angle under aerodynamic force, the higher flexibility also provides an even larger rotation angle under the actuation force, which fortunately increases the final rotation angle or reduces the required actuation force for the same objective angle.

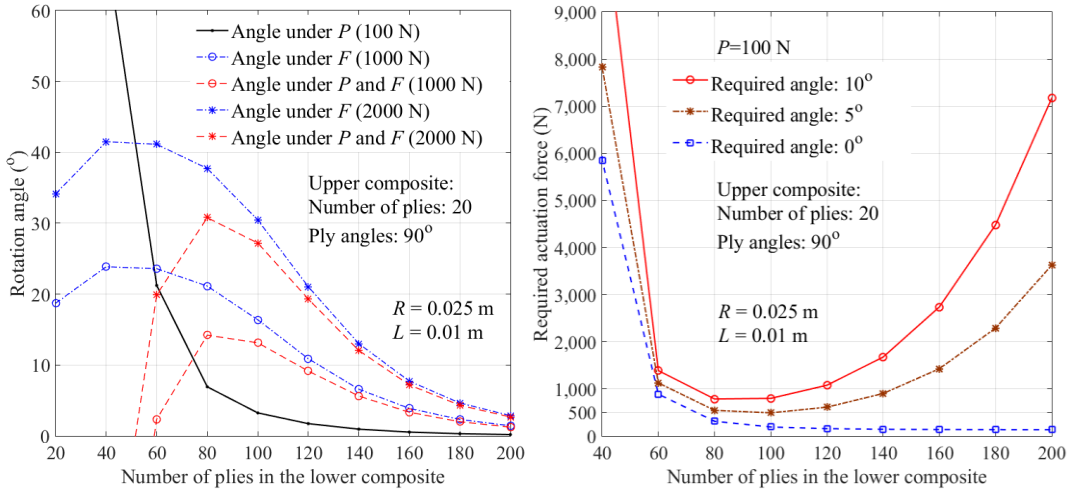

Figure 7. (a) Rotation angle and (b) required force with larger stiffness asymmetry

3.2 Deformation limit of the morphing structure

Another aspect of a morphing structure is its deformation limit. The deformation limit criterion determinates the capability of deformation in the morphing direction, which generally can be expressed as the largest strain the morphing structure can undergo before the structure fails. For the extension morphing the axial deformation limit of the corrugated structure is obtained through the Tsai-Wu criterion [33] and the corrugation structure will be regarded as failed when one layer of the composite starts to fail. The detailed finite element model is built in Abaqus®, and the user subroutine is applied to monitor the stress level and stops the analysis automatically if the stress level exceeds the Tsai-Wu failure envelope. Once the analysis stops, the subroutine will read the current axial displacement, which is then transferred to the axial deformation limit. Figure 8 shows the deformation limit in terms of the radius R and length L as the number of composite plies changes.

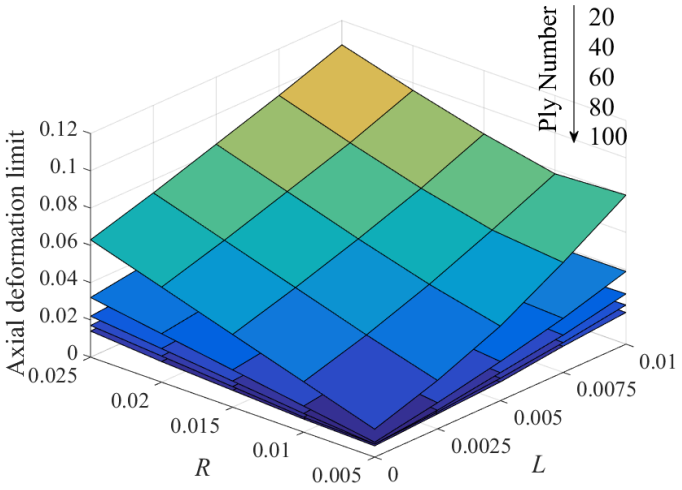

Figure 8. Deformation limit of the round corrugation

The simplified model of the unsymmetrical stiffness structure determines its deformation limit by comparing the axial strain of its upper and lower parts to their corresponding deformation limits. If the axial strains are under their deformation limits, we will assume the structure does not fail.

Figure 9 shows the axial strains compared to their corresponding deformation limits under forces F = 1000 N and P = 100 N. The composite uses the same material data and ply angle as that in section 3.1.

If the deformation is smaller than its limit the corrugation structure is less likely to fail and vice versa. According to the figure, the structural failure is more likely to occur in the upper part since the upper part is more flexible and has a larger axial deformation than the lower part. After the stiffness asymmetry is introduced the lower composite will have a smaller strain than its limit although the deformation limit in the lower composite is also reduced when the number of its plies is increased.

It should be noted that the material properties used in this paper are conservative, and thus larger deformation limits could be available if better material properties are used. Also larger deformation limits can be obtained by changing the composite parameters such as ply angle and thickness. Nevertheless, the above method provides a criterion to design the morphing structure with unsymmetrical stiffness.

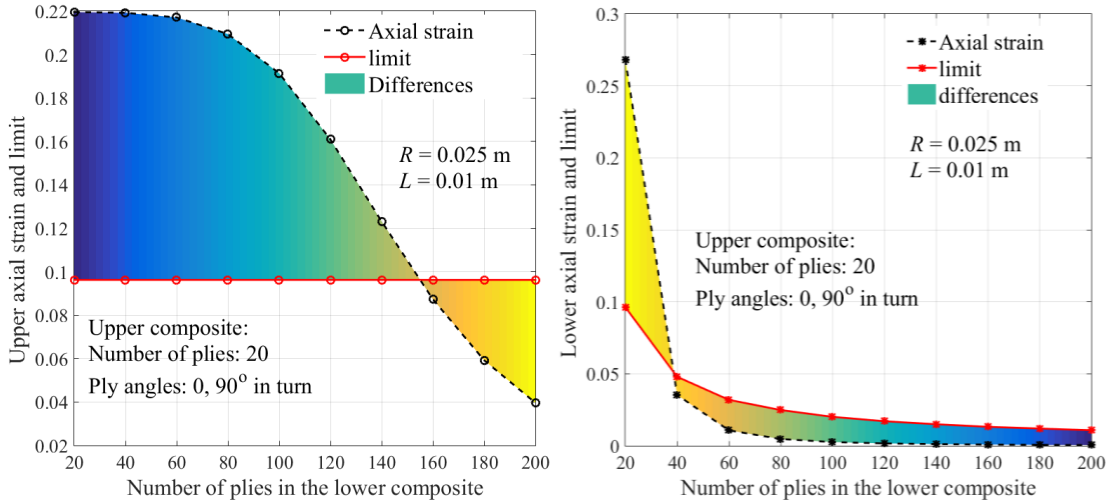

Figure 9. Axial strain compared to its limit, (a): Upper part, (b): Lower part

4. Case study: retrofit of a baseline design

4.1 Baseline design and actuation concept

A baseline design is generated to analyze the basic performance after retrofitting the morphing winglet. Since the paper is focused on the morphing structure, the baseline design is based on the conceptual-level sizing methods from Raymer' book [34]. A twin turboprop airliner is designed as shown in Figure 10.

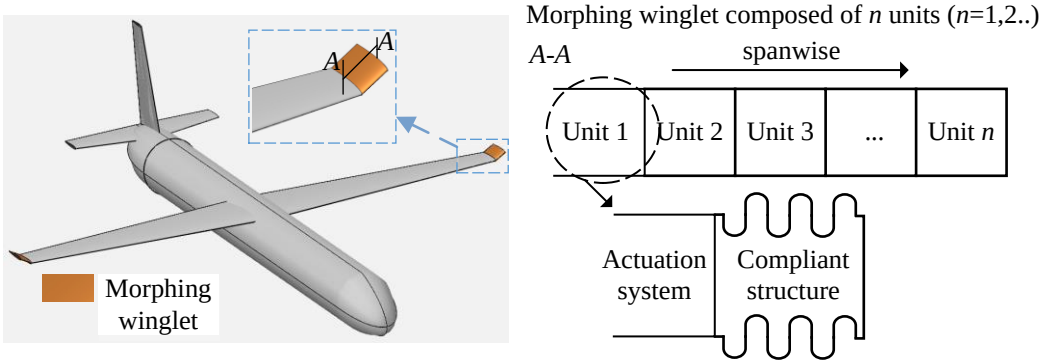

Figure 10. A baseline design with the morphing winglet installed

The conceptual sizing estimates the basic parameters such as the geometrical parameters and weight as

summarized in Table 3. The airfoil is selected from open source data [35] according to the airliner's type.

Number of seats	70	Wing Span (m)	25.38
Range (km)	1500	Wing root chord (m)	3.63
Cruise altitude (m)	4572	Leading edge sweep angle (^{o})	5
Cruise Mach number	0.4	Aspect ratio	10
Take-off gross weight (kg)	27217	Taper ratio	0.4
Empty weight (kg)	12063	Wing tip chord (m)	1.45

Table 3. Baseline design parameters

Figure 10 also shows the morphing winglet retrofitted to the baseline design. The proposed morphing winglet will have the same chord and airfoil as the wing tip. No sweep angle of the winglet will be applied due to the low baseline wing sweep angle and structure simplification. Multiple units of the proposed compliant structure are used to obtain a larger induced deformation. Since the shape change is due to the elastic deformation of the structure rather than rigid rotation, the winglet will be curved during shape change. More complicated wing tip shapes can also be generated when different deformation is required for the multiple units. While the deformation can be accumulated the required actuation force will also be increased due to the reaction force of the following units. As shown in Figure 10, each unit will be composed of two basic parts: the actuation system and the proposed compliant structure. The actuation system will be described later. And the upper and lower surfaces of the compliant structure will be the round corrugation panel.

To provide an adequate deformation limit and reduce the actuation force, the upper ply angle is 90 degrees and the lower ply angle is 0 or 90 degrees in turn. Since the upper surface has a larger deformation, its deformation limit needs to be large enough and the layup of all 90 degrees in the upper ensures the deformation limit is sufficient. Another reason is the more flexible upper layup actually helps to reduce the actuation force as shown in Figures 6 and 7. The geometry of the round corrugation is R = 0.025 m and L = 0.01 m, which ensures the corrugated panel has a large deformation limit as shown in Figure 8. The structure covers the whole chord from the leading edge to the trailing edge, except for some small gaps between the upper and lower surfaces to avoid collision. Those gaps will be filled with soft elastomer whose stiffness can be neglected compared to the structure. Also, the elastomer will fill in the corrugation structure as the skin of the winglet. According to Equation (5), the capability of carrying aerodynamic loads of the proposed compliant structure comes from the actuation force and the stiffness of the structure. Thus, if the elastomer is flexible enough the previous 2D model is useful to calculate the deflection although a method to prevent wrinkling of the soft elastomer is still needed. The width of the compliant structure is 1.45 m. The morphing winglet is assumed to only change its dihedral angle, and thus no twisting is taken into account. Considering the airfoil thickness and space for the actuation system, the height of the compliant structure is equal to 10% of the wing tip chord. Although the constant height does not fully represent the airfoil thickness, it provides a straightforward approach to design the morphing structure if only the change of dihedral angle is expected. The length of one unit compliant structure is assumed to be 0.1 m. The compliant structure is made of the composite described in Table 2, which has 20 plies in the upper panel and 140 in the lower panel. As analyzed above, the actuation force helps to carry the aerodynamic loads. Thus a proper actuation system is essential to the application of the proposed morphing structure. One simple approach is to use a linear actuator which is pinned at the middle between point A and D but

perpendicular to *BC* at point *E*. Another solution could be the use of an air muscle since the air muscle is flexible and can rotate with the structure. Considering the energy cost and stability, it is also necessary for the actuation system to be self-locking.

In this study, an actuation system is proposed based on a worm and rack mechanism. The proposed mechanism provides a solution for the actuation system, and more importantly provides a criterion to estimate the weight of the actuation system. Figure 11(a) shows the schematic of the actuation mechanism. One basic set of the actuation mechanism consists of a worm, a rack and accessories, and multiple sets of the actuation mechanism could be used to represent the change of the actuation force and weight. The worm is installed in a fixed section, and will be actuated by motors to drive the separated rack teeth to slide along the supporting rod *LM*. Different to a conventional rack, the rack here is separated into single teeth, which enables the teeth to rotate with the morphing structure. Then the rack teeth will slide over the point *M* and move to the surface of the internal actuation rod, which is pinned at point *M*. The internal actuation rod is surrounded by the external actuation rod, along which it can slide. In the figure, the compliant structure is represented by the point *A*, *B*, *C* and *D*. Once the rack starts to be in contact with the external rod, beam *BC* will be actuated since it is connected to the external rod.

The proposed mechanism is able to provide an actuation force to beam *BC* and the self-locking feature of the worm can help to save actuation energy. However, the difficulty of the mechanism is the smooth connection between the separated rack teeth and the internal actuation rod. A convey belt might be used to help the transfer over point *M*. Also some accessories are necessary to guarantee the stability of the structure.

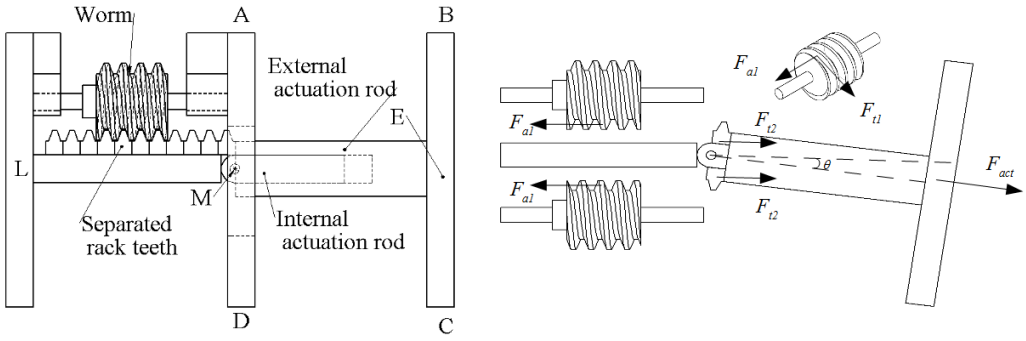

Figure 11. (a) Scheme of proposed actuation system, (b) Forces on the mechanism with two worms

Two pairs of worm and rack drive can be used in one set as shown in Figure 11(b), which can double the actuation force. The relationship between the actuation force and the rated torque can be derived as

$$\begin{aligned} 2F_{t2}\cos\theta &= F_{act} \\ F_{t2} &= F_{a1} \\ F_{t1} &= F_{a1}\tan(\gamma_m + \rho^r) \\ T_1 &= F_{t1}\frac{1}{2}d_{m1} \\ T_r &= f_{safety} * T_1 \end{aligned} \tag{6}$$

where θ is the deflection angle measured from the horizontal line and F_{act} is the actuation force on the beam *BC*. F_{a1} is the axial force of the worm, and F_{t2} is the peripheral force on the rack, which is the reaction force of F_{a1}. F_{t1} is the peripheral force on the worm. The lead angle of the worm γ_m and the reduced friction angle ρ^r can be used to find F_{t1} based on F_{a1}. Then the required torque on the worm T_1

can be obtained from the reference diameter of the worm d_{m1}, after which the rated torque T_r is obtained by including the safety factor f_{safety} (f_{safety} = 1.5).

The maximum actuation force that the mechanism can provide is determined by the maximum loading the worm and rack can bear before failure. The current study determines the strength by considering the tooth root load capacity of the rack, and coefficients obtained in [36] are used. Considering the geometry of the compliant structure, the maximum standard module of the worm is 3 mm with the actuation force equal to 6335.5 N and the rated torque for the motor is 15.3 Nm. More sets of the proposed actuation system can be used, which changes the required actuation force. Although this method will make the maximum actuation force discrete, it is reasonable to provide the boundaries of the actuation force and weight of the actuation system. Taking the geometry constraint into account, the largest number of actuation mechanisms is 16 for the baseline design.

4.2 **Lift to drag ratio and weight estimation**

The proposed application of the compliant structure provides a potential structure solution for the morphing winglet. The morphing winglet could be used to increase span during cruise while remain folded during take-off, landing and taxiing. However, whatever advantages the morphing winglet could bring, one of the side effects is the weight increase due to the installed winglet ΔW_s and actuation system ΔW_a. Generally, the range of the aircraft can be calculated as [34]

$$dR = -\frac{V}{C}\frac{L}{D}\frac{1}{W}dW$$
$$R = \int dR = \frac{V}{C}\frac{L}{D}\ln\left(\frac{W_i}{W_f}\right) \tag{7}$$

where W, V, C are the weight, velocity and specific fuel consumption. The range R is calculated by integration from the initial weight W_i to the final weight W_f. According to this equation, the benefit of a retrofitted morphing winglet, i.e. increased L/D, could be reduced by the increased weight.

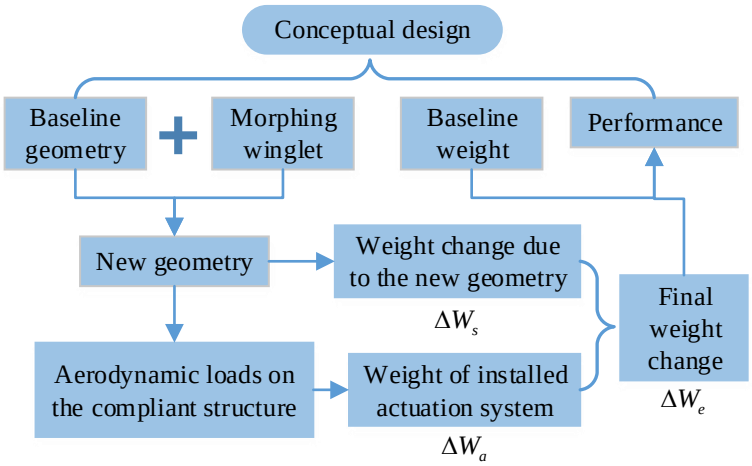

Figure 12. Estimation of weight change

As shown in Figure 12, the weight change due to the installed winglet is calculated by estimating the weight of the new wing geometry since no existing weight data of the unsymmetrical stiffness structure exists. The new wing geometry is defined with winglet dihedral angle equal to zero and its weight is estimated using the following equation [34]:

$$W_{wing} = 0.0051(W_{dg}N_z)^{0.557} S_w^{0.649} A^{0.5} (t/c)_{root}^{-0.4} (1+\lambda)^{0.1} \left(\cos\Lambda\right)^{-1.0} S_{csw}^{0.1} \quad (8)$$

where W_{dg} is the design gross weight of the baseline model. N_z is the ultimate load factor, which is 1.5 times of the design load factor, and the design load factor is taken as 3.5 in this paper. S_w and A are the new wing area and aspect ratio, which include both the wing of the baseline design and the retrofitted winglet. $(t/c)_{root}$ is the airfoil thickness ratio at the wing root. Λ is the sweep angle at 25% of the mean aerodynamic chord. λ is the wing taper ratio and S_{csw} is the control surface area of the wing. All the variables in this equation should be converted to Imperial units before use in this equation.

The weight increase of the actuation system is calculated according to the required actuation force, which is determined by the aerodynamic force on the winglet. The open software AVL [37] is used for the aerodynamic calculation. AVL is based on the vortex lattice method and is linked with Matlab® for modelling and reading outputs. The forces on each element of the winglet are obtained from the output files and summed to get the aerodynamic force on each unit.

Then the required actuation force of each unit is obtained using the method in section 4.1. According to maximum required actuation force of each unit, the number of proposed actuation sets is determined, which is used to estimate the weight of the worm rack mechanism. For the weight of motors, the required actuation force is transferred to the required rated torque. While the weight of motors varies with their type and application scenarios, a commercially available servo motor database [38] is applied for the estimation and the weight of a motor per Newton-Meter is assumed to be 0.093 kg.

The lift to drag ratio is also calculated by AVL. A trade off study is then conducted to show the change of both *L/D* and weight with respect to the number of units of the compliant structure retrofitted.

To represent the change in *L/D*, the reference area is the wing area of the baseline design. From the perspective of the potential applications, the flight condition investigated is when the aircraft just takes off and starts to cruise. The *L/D* is calculated with the dihedral angle of the winglet equal to zero, and the required actuation force is determined when the required angle of each unit is 6 degrees. The weight of the fuel remains the same although the increase of *L/D* could reduce the amount of fuel used. Only the weight change due to the retrofitted winglet and actuation is taken into account.

Figure 13(a) shows the change in *L/D* and gross weight compared to the baseline design. The number of units retrofitted is from 1 to 15, which makes the longest winglet cover 11% of half span. With the increase of the number of units both *L/D* and weight will increase, while the difference between them will increase first until the number of units reaches 10, after which the weight increase will be faster than the *L/D* increase, indicating a negative effect of the winglet if too many units are installed. This could be explained by the increasing required actuation force for each unit, especially the units which are close to the baseline wing tip due to the reaction force of the outboard units. However if the retrofitted winglet is too short, for example when the number of units is equal to 1, the difference between *L/D* and gross weight will also be very small since the effect of the winglet will be negligible compared to the baseline design.

Figure 13(b) shows the required number of actuation sets in each unit with the change of number of units retrofitted, which represents the required actuation force of each unit. The unit number on the *x* axis indicates the location of the winglet, and the direction of the arrow shows the increase of units retrofitted. We can find that after the 8th line in the direction of the arrow, the required number of actuation sets on each unit will not be linear in terms of the winglet unit number, suggesting the

increased required actuation force. According to the geometry constraints, no more than 8 units can be used. Thus, 8 units of compliant structures should be retrofitted considering both the performance and geometry constraint. The deformation of each unit is also within its corresponding limit verified by the method in section 3.2.

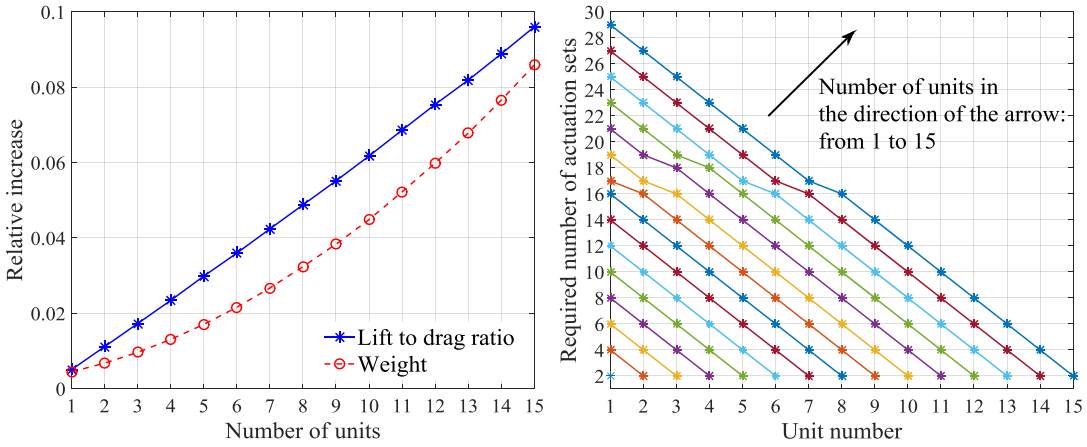

Figure 13. (a) Relative increase of *L*/*D* and weight, (b) Required number of actuation sets

5. Conclusion

To find a solution for spanwise morphing, an innovative compliant structure is proposed making use of the unsymmetrical stiffness of the structure and a conceptual level study is conducted in this paper. The compliant structure consists of the upper and lower parts made of round corrugations. By increasing the stiffness of the lower part, while fixing the stiffness of the upper part, the stiffness asymmetry is increased together with the total stiffness. A simplified 2-dimensional model is built to estimate the deformation of the structure analytically.

From the above analysis, we can conclude that the final deformation of the structure is determined by the total stiffness, stiffness asymmetry, aerodynamic loads and actuation force. By allocating unsymmetrical stiffness into the morphing structure we can achieve rotation deformation for the structure from linear actuation. Furthermore, while the increasing total stiffness of the structure can help to carry aerodynamic loads, the stiffness asymmetry is also able to induce a large rotation angle in the opposite direction. With adequate total stiffness and properly selected stiffness asymmetry the morphing structure is able to carry aerodynamic loads and change its shape simultaneously. Also the method to determine whether the morphing structure will fail is developed by comparing the axial deformation of the upper and lower parts to the corresponding deformation limit separately.

The morphing winglet benefits from the unsymmetrical stiffness of the morphing structure. By increasing the total stiffness of the structure and allocating the unsymmetrical stiffness simultaneously, the novel compliant structure helps to reduce the requirement of the actuation system and provides a solution to the morphing skin inherently. Since only a linear actuation force is required, a large range of actuation systems can be applied including a conventional actuator, which can be more reliable.

With the help of this simplified model, the application of the morphing structure is investigated showing the potential pros and cons. A baseline design is generated to provide the basic information for comparison. A basic actuation mechanism is also introduced to provide the solution for constant actuation as well as weight estimation.

Finally the change of lift to drag ratio and weight are analyzed with different numbers of units

retrofitted to the baseline design. It is found after a critical point the increase of weight will be faster than the increase of lift to drag ratio. Also the geometry of the baseline design constrains the number of actuation sets. Thus, a trade-off selection should be made according to the situation. In this case, 8 units of morphing structure are used, increasing the lift to drag ratio by about 5% and the weight by about 3.5%.

Although the aerodynamic performance improvement is partially balanced by the weight increase, other functions of the morphing winglet, such as load alleviation, reducing span during take-off and landing and even flight control can be introduced with the morphing structure. Furthermore if 3-dimensional deformation is considered the winglet twist angle can also be changed together with its dihedral angle.

In summary, the novel concept of a compliant structure provides a solution to change the dihedral angle of a morphing winglet. This preliminary study has shown its properties and potential applications. Future work will continue on the optimization and experimental testing of the structure.

6. Acknowledgment

Chen Wang would like to thank the China Scholarship Council (CSC) and the College of Engineering of Swansea University for providing his PhD scholarship.

7. References

1. Gilbert, W. W., *Mission adaptive wing system for tactical aircraft.* Journal of Aircraft, 1981. **18**(7): p. 597-602.

2. Ajaj, R. M., E. S. Flores, M. I. Friswell, et al., *The Zigzag wingbox for a span morphing wing*. Aerospace Science and Technology, 2013. **28**(1): p. 364-375.

3. Ajaj, R., M. I. Friswell, E. I. S. Flores, et al., *An integrated conceptual design study using span morphing technology.* Journal of Intelligent Material Systems and Structures, 2014. **25**(8): p. 989-1008.

4. Kudva, J., *Overview of the DARPA smart wing project.* Journal of Intelligent Material Systems and Structures, 2004. **15**(4): p. 261-267.

5. Woods, B. K. S., O. Bilgen, and M. I. Friswell, *Wind tunnel testing of the fish bone active camber morphing concept.* Journal of Intelligent Material Systems and Structures, 2014. **25**(7): p. 772-785.

6. Bowman, J., B. Sanders, B. Cannon, et al., *Development of Next Generation Morphing Aircraft Structures*. In: *Proceedings of 48th AIAA/ASME/ASCE/AHS/ASC Structures, Structural Dynamics, and Materials Conference*, 23-26 April, 2007, Honolulu, Hawaii, AIAA 2007-1730.

7. Andersen, G. R., D. L. Cowan, and D. J. Piatak, *Aeroelastic modeling, analysis and testing of a morphing wing structure*. In: *Proceedings of 48th AIAA/ASME/ASCE/AHS/ASC Structures, Structural Dynamics, and Materials Conference*, 23-26 April, 2007, Honolulu, Hawaii, AIAA 2007-1734.

8. Whitcomb, R. T., *A design approach and selected wind tunnel results at high subsonic speeds for wing-tip mounted winglets.* 1976, NASA Langley Research Center, Hampton, NASA TN D-8260.

9. Bourdin, P., A. Gatto, and M. I. Friswell, *The application of variable cant angle winglets for morphing aircraft control*. In: *Proceedings of 24th Applied Aerodynamics Conference*, 5-8 June, 2006, San Francisco, California, AIAA 2006-3660.

10. Bourdin, P., A. Gatto, and M. I. Friswell, *Aircraft control via variable cant-angle winglets.* Journal of Aircraft, 2008. **45**(2): p. 414-423.

11. Falcão, L., A. A. Gomes, and A. Suleman, *Aero-structural design optimization of a morphing wingtip.* Journal of Intelligent Material Systems and Structures, 2011. **22**(10): p. 1113-1124.

12. Gomes, A. A., L. Falcao, and A. Suleman, *Study of an articulated winglet mechanism*. In: *Proceedings of 54th AIAA/ASME/ASCE/AHS/ASC Structures, Structral Dynamics, and Materials Conference*, April 8-11, 2013, Boston, Massachusetts, AIAA 2013-1452.
13. Smith, D. D., R. Ajaj, A. T. Isikveren, et al., *Multi-objective optimization for the multiphase design of active polymorphing wings.* Journal of Aircraft, 2012. **49**(4): p. 1153-1160.
14. Smith, D. D., M. H. Lowenberg, D. P. Jones, et al., *Computational and Experimental Validation of the Active Morphing Wing.* Journal of Aircraft, 2014. **51**(3): p. 925-937.
15. Guo, S., J. Espinosa De Los Monteros, and Y. Liu, *Gust Alleviation of a Large Aircraft with a Passive Twist Wingtip.* Aerospace, 2015. **2**(2): p. 135-154.
16. Castrichini, A., V. Hodigere Siddaramaiah, D. E. Calderon, et al., *Nonlinear Folding Wing Tips for Gust Loads Alleviation.* Journal of Aircraft, 2016.
17. Li, W., K. Xiong, H. Chen, et al., *Research on variable cant angle winglets with shape memory alloy spring actuators.* Acta Aeronautica et Astronautica Sinica, 2012. **33**(1): p. 22-33.
18. Daniele, E., A. De Fenza, and P. Della Vecchia, *Conceptual adaptive wing-tip design for pollution reductions.* Journal of Intelligent Material Systems and Structures, 2012. **23**(11): p. 1197-1212.
19. Mattioni, F., P. M. Weaver, M. I. Friswell, et al., *Modelling and applications of thermally induced multistable composites with piecewise variation of lay-up in the planform*. In: *Proceedings of 48th AIAA/ASME/ASCE/AHS/ASC Structures, Structural Dynamics and Materials Conference*, 23-26 April, 2007, Honolulu, Hawaii, AIAA 2007-2262.
20. Mattioni, F., P. M. Weaver, K. D. Potter, et al., *The application of thermally induced multistable composites to morphing aircraft structures*. In: *Proceedings of Industrial and Commercial Applications of Smart Structures Technologies*, 09 March, 2008, San Diego, California: International Society for Optics and Photonics, Proc. of SPIE Vol.6930 693012.
21. Wang, C., H. H. Khodaparast, and M. I. Friswell, *Investigating the benefits of morphing wing tip devices-A case study*. in *International Forum on Aeroelasticity and Structure Dynamics*. June 28-July 02, 2015. Saint Petersburg, Russia.
22. Skillen, M. D. and W. A. Crossley, *Morphing Wing Weight Predictors and their Application in a Template-Based Morphing Aircraft Sizing Environment II, Part II: Morphing Aircraft Sizing via Multi-Level Optimization.* 2008, NASA Report, CR-2008-214903.
23. Park, P. S. and K. Rokhsaz, *Effects of a winglet rudder on lift-to-drag ratio and wake vortex frequency*. In: *Proceedings of 21st applied aerodynamics conference*, 23-26 June, 2003, Orlando, Florida, AIAA 2003-4069.
24. Kauertz, S. and G. Neuwerth, *Excitation of instabilities in the wake of an airfoil by means of active winglets.* Aerospace science and technology, 2006. **10**(7): p. 551-562.
25. Jingeleski, D. J., J. A. Schetz, and R. Kapania, *Aerodynamic Analysis of Variable Geometry Raked Wingtips for Mid-Range Transonic Transport Aircraft*. In: *Proceedings of 31st AIAA Applied Aerodynamics Conference*, June 24-27, 2013, San Diego, California: American Institute of Aeronautics and Astronautics, AIAA 2013-2403.
26. Dadeppo, D. A., *Introduction to structural mechanics and analysis*. 1999, Upper Saddle River, N.J.: Prentice Hall.
27. *Matlab R2014b*, 2014, The MathWorks Inc.
28. *ABAQUS 6.13*, 2013, Dassault Systèmes
29. Kaw, A. K., *Mechanics of composite materials*. Second ed. 2010, Boca Raton: CRC press.
30. Thill, C., J. A. Etches, I. P. Bond, et al., *Composite corrugated structures for morphing wing skin*

applications. Smart Materials and Structures, 2010. **19**(12): p. 124009-124018.

31. Dayyani, I., M. I. Friswell, S. Ziaei-Rad, et al., *Equivalent models of composite corrugated cores with elastomeric coatings for morphing structures.* Composite Structures, 2013. **104**: p. 281-292.

32. Xia, Y., M. I. Friswell, and E. I. S. Flores, *Equivalent models of corrugated panels.* International Journal of Solids and Structures, 2012. **49**(13): p. 1453-1462.

33. Tsai, S. W. and E. M. Wu, *A general theory of strength for anisotropic materials.* Journal of composite materials, 1971. **5**(1): p. 58-80.

34. Raymer, D. P., *Aircraft Design: A conceptual Approach*. Fourth ed. 2006, Virginia: American Institute of Aeronautics and Astronautics.

35. Group, U. a. A., *UIUC Airfoil Coordinates Database*, 2015.

36. Jelaska, D. T., *Gears and gear drives*, 2012, John Wiley & Sons.

37. Drela, M. *AVL*. 2015; Available from: http://web.mit.edu/drela/Public/web/avl/.

38. Marketplace, T. R. *Invenscience i00600 Torxis Servo* 2015; Available from: http://www.robotmarketplace.com/products/0-PL1390.html.

8. Appendix

This appendix shows the calculation of displacements of the proposed compliant structure due to the actuation force. Since the upper and lower beams are fixed, there are six unknown reaction forces and the moments as shown in Figure A1, which are related to only three independent equations of equilibrium; thus structure is statically indeterminate. The reaction forces applied at point *D* are chosen as redundant reactions. Then the structure becomes statically determinate with X_1, X_2, X_3 applied at point *D*.

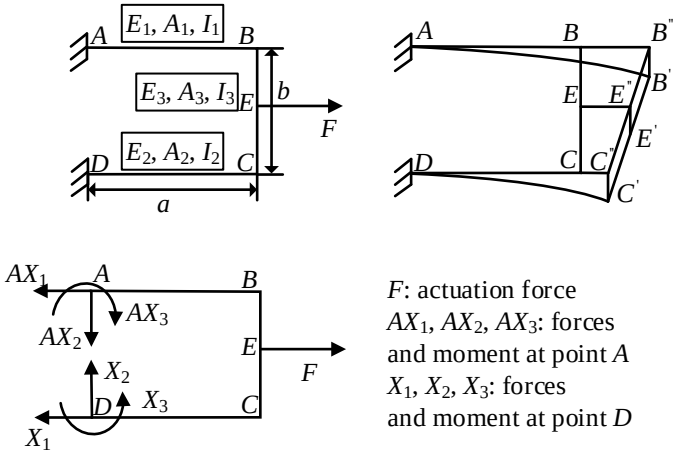

Figure A1. Loads at point *A*, *D* and the geometry relationship of point *B*, *C*, and *E*

To satisfy the original boundary condition, the redundant reactions will make the horizontal displacement *u*, vertical displacement *v* and rotation α at point *D* zero. Using the principle of superposition, *u* can be expressed as

$$u = u_F + u_{X_1} + u_{X_2} + u_{X_3} \tag{1}$$

where u_F is horizontal displacement caused by the actuation force *F* alone, and u_{X_i} $(i = 1, 2, 3)$ is the horizontal displacement caused by the reaction X_i alone.

According to the principle of virtual work, the displacement under an external load can be expressed as

$$u = \sum\int \frac{mM}{EI}dx + \sum\int \frac{nN}{EA}dx \tag{2}$$

where M and N are the bending moment and axial force under the external load, and m and n are the bending moment and axial force under the unit load applied in the same direction as the required displacement. Figure A2 shows the internal bending moment and axial force caused by F and the unit load, which is in the same direction to X_i (i=1, 2, 3). Thus, using the above equation, we obtain

$$\begin{aligned} u_F &= \sum\int \frac{mM}{EI}dx + \sum\int \frac{nN}{EA}dx \\ &= \int_0^a \frac{-b\cdot(\frac{1}{2}Fb)}{E_1I_1}dx + \int_0^a \frac{-1\cdot F}{E_1A_1}dx \\ &= -\frac{Fa}{E_1A_1} - \frac{Fab^2}{2E_1I_1} \end{aligned} \tag{3}$$

$$\begin{aligned} u_{X_1} &= \int_0^a \frac{1\cdot X_1}{E_1A_1}dx + \int_0^a \frac{1\cdot X_1}{E_2A_2}dx + \int_0^a \frac{b\cdot bX_1}{E_1I_1}dx \\ &= (\frac{a}{E_1A_1} + \frac{a}{E_2A_2} + \frac{ab^2}{E_1I_1})X_1 \end{aligned} \tag{4}$$

The same method can be used to obtain the other components of u, as well as the vertical displacement v and rotation α. Finally, at point D we obtain

$$\begin{aligned} u &= -\frac{Fa}{E_1A_1} - \frac{Fab^2}{2E_1I_1} + (\frac{ab^2}{E_1I_1} + \frac{a}{E_1A_1} + \frac{a}{E_2A_2})X_1 + \frac{a^2b}{2E_1I_1}X_2 - \frac{ab}{E_1I_1}X_3 \\ v &= -\frac{a^2b}{4E_1I_1}F + \frac{a^2b}{2E_1I_1}X_1 + (\frac{a^3}{3E_1I_1} + \frac{a^3}{3E_2I_2})X_2 - (\frac{a^2}{2E_1I_1} + \frac{a^2}{2E_2I_2})X_3 \\ \alpha &= \frac{Fab}{2E_1I_1} - \frac{ab}{E_1I_1}X_1 - (\frac{a^2}{2E_1I_1} + \frac{a^2}{2E_2I_2})X_2 + (\frac{a}{E_1I_1} + \frac{a}{E_2I_2})X_3 \end{aligned} \tag{5}$$

Making the displacement and rotation at point D zero, the redundant reactions can be solved to give

$$\begin{aligned} X_1 &= \frac{E_2A_2(E_1A_1b^2 + 2E_1I_1 + 2E_2I_2)}{(E_1^2A_1I_1 + E_2^2A_2I_2 + E_1E_2A_1I_2 + E_1E_2A_2I_1 + E_1E_2A_1A_2b^2)}\frac{F}{2} \\ X_2 &= 0 \\ X_3 &= -\frac{E_2I_2(E_1A_1 - E_2A_2)}{(E_1^2A_1I_1 + E_2^2A_2I_2 + E_1E_2A_1I_2 + E_1E_2A_2I_1 + E_1E_2A_1A_2b^2)}\frac{Fb}{2} \end{aligned} \tag{6}$$

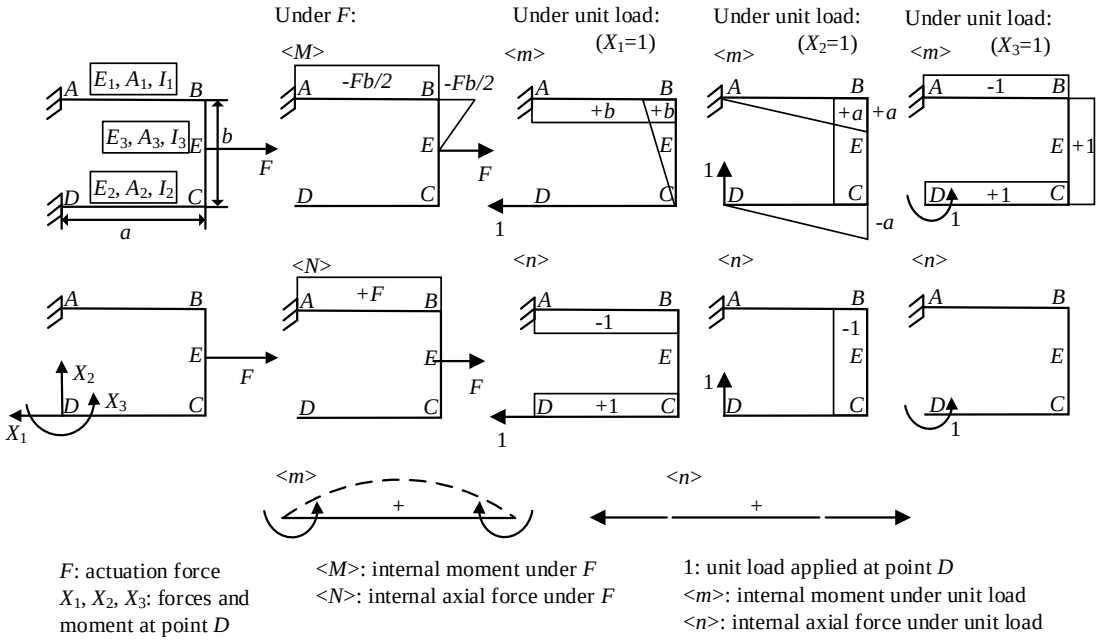

Figure A2. Internal loads under the actuation force F

Then, we can obtain the reactions at point A from the equations of equilibrium as shown in Figure A3.

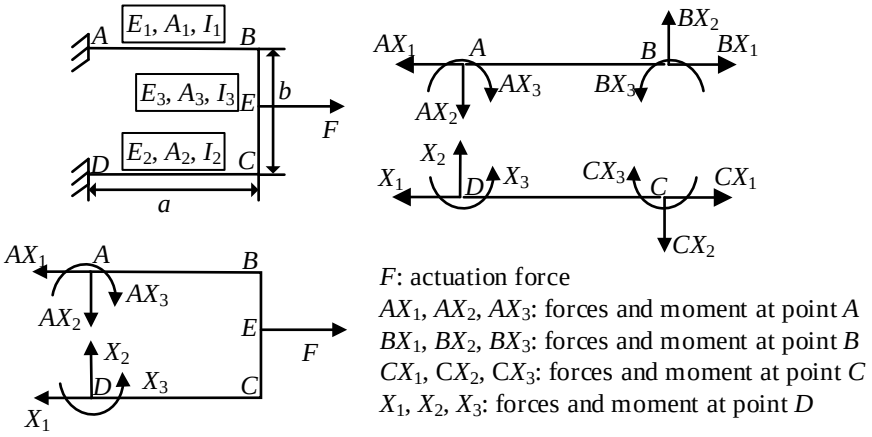

Figure A3. Balanced structure and beam AB and DC

According to the equilibrium of the whole structure,

$$\begin{aligned} F - AX_1 - X_1 &= 0 \\ AX_2 - X_2 &= 0 \\ AX_3 + X_1 b - \frac{1}{2} Fb - X_3 &= 0 \end{aligned} \tag{7}$$

Thus,

$$\begin{aligned} AX_1 &= \frac{E_1 A_1 (E_2 A_2 b^2 + 2E_1 I_1 + 2E_2 I_2)}{(E_1^2 A_1 I_1 + E_2^2 A_2 I_2 + E_1 E_2 A_1 I_2 + E_1 E_2 A_2 I_1 + E_1 E_2 A_1 A_2 b^2)} \frac{F}{2} \\ AX_2 &= 0 \\ AX_3 &= \frac{E_1 I_1 (E_1 A_1 - E_2 A_2)}{(E_1^2 A_1 I_1 + E_2^2 A_2 I_2 + E_1 E_2 A_1 I_2 + E_1 E_2 A_2 I_1 + E_1 E_2 A_1 A_2 b^2)} \frac{Fb}{2} \end{aligned} \tag{8}$$

Applying the equations of equilibrium to the upper and lower beams separately gives the internal forces

and moments at point *B* and *C*, after which the displacements of point *B* and *C* can be obtained.

For the upper beam *AB*:

$$\begin{aligned} BX_1 - AX_1 &= 0 \\ AX_2 - BX_2 &= 0 \\ AX_3 - BX_3 - BX_2 a &= 0 \end{aligned} \tag{9}$$

$$\begin{aligned} u_B &= BX_1 a / (E_1 A_1) \\ v_B &= -BX_3 a^2 / (2E_1 I_1) - BX_2 a^3 / (3E_1 I_1) \end{aligned} \tag{10}$$

So,

$$\begin{aligned} u_B &= \frac{a\left[F - E_2 A_2 F(E_1 A_1 b^2 + 2E_1 I_1 + 2E_2 I_2)/(2K_t)\right]}{E_1 A_1} \\ &= \frac{F}{2} a \frac{2E_1 I_1 + 2E_2 I_2 + E_2 A_2 b^2}{K_t} \\ v_B &= \frac{a^2 \frac{Fb}{2}\left[E_2 A_2 (E_1 A_1 b^2 + 2E_1 I_1 + 2E_2 I_2)/K_t - 1 + E_2 I_2 (E_1 A_1 - E_2 A_2)/K_t\right]}{2E_1 I_1} \\ &= \frac{Fb}{2} a^2 \frac{E_2 A_2 - E_1 A_1}{2K_t} \\ K_t &= E_1 A_1 E_1 I_1 + E_2 A_2 E_2 I_2 + E_1 A_1 E_2 I_2 + E_1 I_1 E_2 A_2 + E_1 A_1 E_2 A_2 b^2 \end{aligned} \tag{11}$$

Here, the term K_t is the combination of axial and bending stiffnesses of the upper and lower beams, and the term E_2A_2-E_1A_1 is the difference of the axial stiffnesses.

For the lower beam *DC*:

$$\begin{aligned} CX_1 - X_1 &= 0 \\ CX_2 - X_2 &= 0 \\ CX_3 + CX_2 a - X_3 &= 0 \end{aligned} \tag{12}$$

$$\begin{aligned} u_C &= \frac{CX_1 a}{E_2 A_2} \\ v_C &= \frac{CX_3 a^2}{2E_2 I_2} + \frac{CX_2 a^3}{3E_2 I_2} \end{aligned} \tag{13}$$

Thus

$$\begin{aligned} u_C &= \frac{F}{2} a \frac{2E_1 I_1 + 2E_2 I_2 + E_1 A_1 b^2}{K_t} \\ v_C &= \frac{Fb}{2} a^2 \frac{E_2 A_2 - E_1 A_1}{2K_t} \end{aligned} \tag{14}$$

Point *E* is the midpoint of beam *BC*. As shown in Figure A1, BB'', CC'', EE'' are the horizontal displacements of points *B*, *C* and *E* respectively, and $B''B'$, $E''E'$, $C''C'$ are the vertical displacements of points *B*, *C* and *E*. According to the geometry relationship,

$$
\begin{aligned}
u_E &= \frac{u_B + u_C}{2} \\
&= \frac{F}{2} a \frac{2E_1 I_1 + 2E_2 I_2 + b^2 (E_1 A_1 + E_2 A_2)/2}{K_t} \\
v_E &= \frac{v_B + v_C}{2} \\
&= \frac{Fba^2}{2} \frac{E_2 A_2 - E_1 A_1}{2K_t}
\end{aligned}
\tag{15}
$$